E3259

# Modeling the Radiolytic Corrosion of Fractured Nuclear Fuel under Permanent Disposal Conditions

**Linda Wu,*** **Nazhen Liu, Zack Qin, and David W. Shoesmith**\*\*,z

*Department of Chemistry and Surface Science Western, The University of Western Ontario, London, Ontario N6A 5B7, Canada*

A two-dimensional model has been developed to simulate the corrosion of nuclear fuel pellets under permanent waste disposal conditions in a steel vessel with a corrosion-resistant copper shell. The primary emphasis was on the corrosion behavior within cracks with various dimensions. It was shown that a simplified α-radiolysis model which only accounts for the radiolytic production of $H_2O_2$ and $H_2$ provides a reasonably accurate simulation and is a time-efficient alternative to the use of a model including a full α-radiolysis reaction set. Both radiolytic $H_2O_2$ and $H_2$ can accumulate inside the cracks. However, the $[H_2O_2]$ is regulated by its reaction with $UO_2$ to cause corrosion and especially its decomposition to $O_2$ and $H_2O$. This leads to $[H_2]$ much greater than $[H_2O_2]$ within the cracks. The critical $[H_2]$, $[H_2]_{crit}$, required to completely suppress corrosion has been calculated for various crack widths and depths. The maximum $[H_2]_{crit}$ is only ∼ 12 times that required on a planar surface irrespective of the dimensions of the crack. The build up of $H_2$ within cracks is effectively a shift to more reducing conditions. As a consequence, the redox conditions within cracks begin to decouple from the external redox conditions. This makes the fuel corrosion process at these locations less sensitive than might be expected to the influences of the $H_2$ and $Fe^{2+}$ produced by corrosion of the steel vessel.

The recommended approach for the long-term management of used nuclear fuel in Canada is adaptive phased management, and includes centralized containment and the isolation of the used fuel in a deep geological repository. As accepted internationally, the repository concept is based on multiple barriers including the fuel bundles, durable metal containers with an outer barrier of copper and an inner carbon steel vessel, a clay buffer and seals around the container, and a deep geologic environment.[1] A key barrier is the corrosion-resistant container that is expected to isolate the used fuel for a very long time.[2,3] However, it is judicious to examine the consequences of container failure and the exposure of used fuel bundles to groundwater. In the anoxic conditions anticipated in a deep geological repository, water radiolysis will be the only source of oxidants resulting from the radiation fields associated with the used fuel. The key radiolysis product, $H_2O_2$, has been shown to be the primary oxidant driving fuel corrosion.[4–6] Oxidation of fuel ($U^{IV}$) will produce the oxidized form ($U^{VI}$) with a considerably higher solubility leading to the release of radionuclides. Another corrosion front, sustained by water reduction to produce the potential redox scavengers, $Fe^{2+}$ and $H_2$, is present on the inner surface of the carbon steel vessel. A series of experimental studies and model simulations[7–10] suggest that a complex series of homogeneous solution reactions and heterogeneous surface reactions can significantly influence the fuel corrosion process.

The inhibition effect of $H_2$ on the fuel corrosion is an important factor in the safety assessment of a deep geological disposal site. The primary source of $H_2$ is the anaerobic corrosion of the steel vessel, and a secondary source is the radiolysis of water.[11] Hydrogen has been shown to suppress $UO_2$ corrosion on a range of $UO_2$ materials from spent fuel itself to α-doped $UO_2$ and simulated fuels (SIMFUELs).[8,12–14] SIMFUELs are $UO_2$ matrices doped with a series of stable elements in the proportions required to simulate the chemical effects of in-reactor irradiation.[15] In particular, they contain the rare earth dopants that influence the chemical reactivity of the $UO_2$ matrix and the noble metal (ε) particles observed to separate within the $UO_2$ matrix.[16,17] Corrosion studies using irradiated spent fuel segments[18–21] showed that dissolved $H_2$ (in the concentration range 1 to 42 mmol $L^{-1}$) inhibited fuel dissolution. Cera et al.[22] observed in a long-term fuel leaching experiment that even radiolytically produced $H_2$ alone

could inhibit fuel corrosion. Traboulsi et al.[23] recently performed a corrosion experiment on $UO_2$ in distilled water externally α-irradiated in either an open or closed atmosphere. The difference between these conditions was that the radiolytic $H_2$ would be evacuated in an open atmosphere but would accumulate in the closed system. In the closed system the dissolved U concentration was suppressed by $H_2$ to about one third of that observed in the open system.

In electrochemical experiments Broczkowski and co-workers observed a suppression of the corrosion potential by $H_2$ leading to a decrease in extent of surface oxidation on SIMFUEL.[24–26] The extent of this effect was found to depend on the number density of noble metal (ε) particles in the SIMFUEL pellets and the concentration of dissolved $H_2$. It was proposed that fuel corrosion was suppressed by $H_2$ oxidation on the ε-particles galvanically coupled to the fission-product-doped $UO_{2+x}$ matrix. Other possible mechanisms by which $H_2$ can suppress the corrosion reaction include scavenging the radiolytic $H_2O_2$[27–29] and reducing the dissolved $UO_2^{2+}$.[30,31] These and other experiments[14,32] have investigated the kinetics of related reactions to facilitate the prediction of fuel corrosion rates.

Based on experimental data, several predictive modeling approaches have been recently developed to describe the $H_2$ effect involved in spent fuel dissolution.[10] Jonsson et al.[33] developed a comprehensive model which integrated the kinetic data and tried to account for the geometrical distribution of radiation dose rate and the effects of the oxidant scavengers $Fe^{2+}$ and $H_2$, fuel burnup, and ground water chemistry. The $H_2$ pressure required to suppress fuel corrosion under Swedish repository conditions was calculated. It was also concluded that in the presence of sufficient $Fe^{2+}$, its effect plus that of the radiolytically produced $H_2$ alone, could effectively inhibit fuel corrosion. Based on recently available kinetic data, Trummer et al.[28] and Wu et al.[34] also calculated the critical $[H_2]$ required to suppress α-radiolytically-induced $UO_2$ corrosion, in a closed and an open (connected to ground water) system, respectively. In both cases, the $UO_2$ corrosion rate was found to be very sensitive to the $[H_2]$.

These and other radiolytic models (in particular for α-radiolysis) for spent fuel corrosion[10,35–38] put emphasis on the spatial distribution of radiolytic species since all the α-particle energy is deposited within a few tens of micrometers of the fuel/solution interface. Consequently, mass transport becomes important in coupling the homogeneous aqueous reactions and heterogeneous surface processes involved. This is especially important if the influence of container corrosion products, $Fe^{2+}$ and $H_2$, on the redox conditions at the fuel surface are to be

quantitatively modeled. Therefore, a common approach adopted in these models is the use a 1-dimensional arrangement to simulate the radiolytic corrosion of a planar fuel surface, as opposed to a zero-dimensional arrangement which would only be suitable for homogeneous systems (e.g., γ-radiolysis).

However, a 1-dimensional arrangement cannot account for the complex geometry of spent fuel, in particular, pellet cracking. The irradiated fuel pellets are extensively fractured due to stress from thermal tension during in-reactor irradiation and the cooling process, or due to defects introduced during sintering and densification.[39–44] In addition, a large number of fission gas bubbles /tunnels are formed along $UO_2$ grain boundaries.[4,45–48] These structures will provide primary pathways for groundwater, extending the α-radiolysis region and leading to the local accumulation of radiolytic species, while the externally produced $Fe^{2+}$ and $H_2$ may have limited access to these potentially reactive locations. Such geometric effects could, therefore, have a significant impact on the overall ability of container corrosion products to influence fuel corrosion and radionuclide release.

In this paper, we extend the previous 1-D model[34,49] to the 2-D case and focus on the behavior expected within groundwater-flooded cracks. We examine different crack dimensions and their effect on local radiolysis and, consequently, the fuel corrosion rate. The efficiency of steel corrosion products, $H_2$ in particular, in suppressing the fuel corrosion is also evaluated. The eventual goal is to develop a model to determine how different types of fuel cladding failure will influence the interaction between the two corrosion fronts (on the fuel and steel vessel surfaces).

## Model Description

After in-reactor irradiation, the properties of the $UO_2$ matrix are substantially changed by the presence of rare earth elements and noble metal (ε) particles.[7] The rare earth elements ($Re^{III}$) in the fuel lattice lead to an increase in the conductivity, and the noble metal particles, segregated at grain boundaries, can act as either cathodes or anodes (depending on the prevailing redox conditions) galvanically-coupled to the conductive doped $UO_2$ matrix.

Fig. 1 illustrates the two corrosion fronts and main reactions involved. The model includes: (1) the production of $H_2O_2$ and $H_2$ by water radiolysis; (2) the oxidative dissolution (corrosion) of $UO_2$ supported by $H_2O_2$ reduction on both the $UO_2$ surface (reaction 2a) and noble metal particles (reaction 2b); (3) the reduction of oxidized surface species ($U^V/U^{VI}$) by $H_2$ oxidation on noble metal particles (reaction 3a) and of dissolved $UO_2^{2+}$ either by reaction with $H_2$ in so-

lution (reaction 3b) or with $H_2$ catalyzed on the fuel surface (reaction 3c); (4) the reaction of $H_2O_2$ with $H_2$ catalyzed by noble metal particles; (5) the scavenging of $H_2O_2$ in homogeneous solution by reaction with $Fe^{2+}$; and (6) the decomposition of $H_2O_2$ to $O_2$ and $H_2O$ (not shown in Fig. 1). The details of these reactions have been described elsewhere.[34]

Since the groundwater between the two corrosion fronts, Fe and $UO_2$, is stagnant and contains an excess of inert ions, e.g., $Na^+$ and $Cl^-$, the rates of the various processes in the model can be considered governed by a series of diffusion-reaction equations. At steady state, a balance will be established between the diffusion and reaction processes, Eq. 1,

$$D_i \left[ \frac{\partial^2 c_i}{\partial x^2} + \frac{\partial^2 c_i}{\partial y^2} \right] = - \sum_k R_k(i) \qquad [1]$$

where $c_i$ and $D_i$ are the concentration and diffusion coefficient of species $i$, respectively, and $R_k(i)$ is the reaction rate of species $i$ in homogeneous reaction $k$, such as reactions 1, 3b, 5, and 6a.[34] If $i$ is a product in the reaction $k$, $R > 0$; on the other hand, if $i$ is a reactant, $R < 0$. The boundary conditions are defined by the surface reactions (2a, 2b, 3a, 3c, 4, and 6b), as described in detail previously.[34]

The 2-D model arrangement adopted for the simulation of a fuel crack and the fuel/groundwater interface is illustrated in Fig. 2. A simplified rectangular geometry is adopted for the cross section, and the dimension of the crack is determined by its width and depth. Alpha particle emission is assumed to occur uniformly across the complete surface which can be considered wrapped in a thin radiation zone. The diffusion zone is defined as a water layer on the fuel surface, over which species can diffuse to, or from, the fuel surface. Beyond this zone, uniform concentrations are presumed to prevail.

Radiolysis is considered to occur uniformly within a thin layer of solution on the fuel surface with a thickness, $b = 13$ μm, given by the average penetration distance of α-radiation in water.[50] Beyond this layer no radiolysis products are produced. Previous calculations demonstrated that this approach provides a simple, but reasonably accurate alternative to the actual radiolysis effect in which α-particles lose energy non-uniformly along the water penetration path.[49,51] The boundary of the uniform radiation zone on the fuel surface is indicated by dashed lines in Fig. 2. Using this simplification, the dose rate is uniformly distributed across the surface except in the corners at the base of the crack. These locations experience a radiation dose rate double that on flat surfaces. The corners at the top of the crack are assumed to experience the same dose rate as the flat surface. The
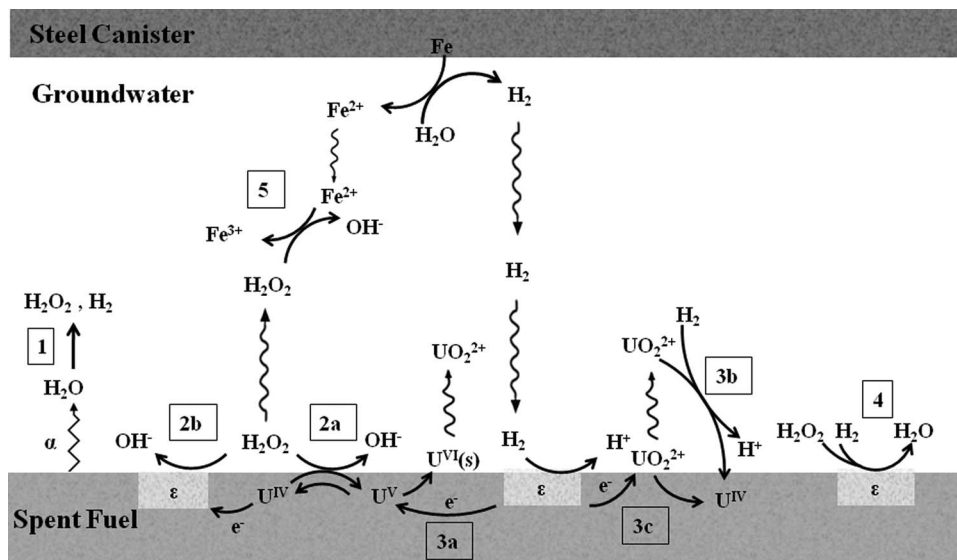


**Figure 1.** Reactions included in the model for the α-radiolytic corrosion of spent nuclear fuel. This diagram is adapted from previous work.[34]
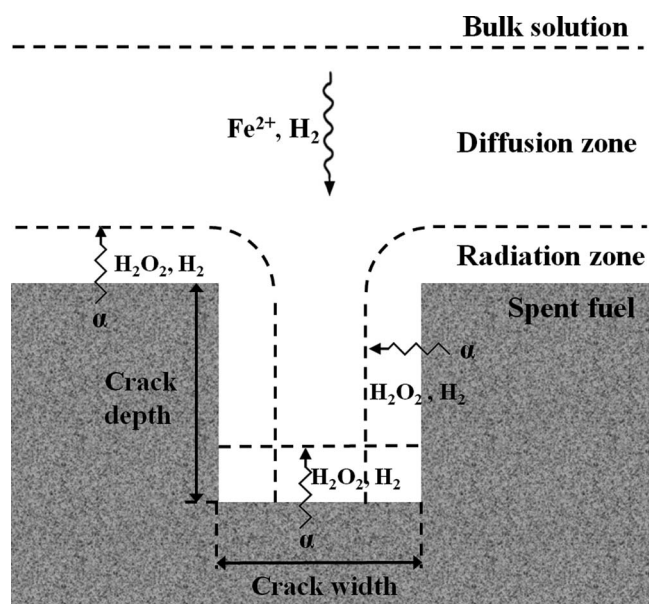
**Figure 2.** Model arrangement showing a cross section of the fuel/solution interface for the simulation of radiolytic corrosion inside a crack in a fuel pellet.

average alpha dose rate used in all calculations is $9.03 \times 10^5$ Gy a$^{-1}$[50] corresponding to CANDU fuel with a burnup of 220 MWh kgU$^{-1}$ at 1000 years after discharge from reactor.

## Results and Discussion

The mathematical model is numerically solved using COMSOL Multiphysics based on the finite element method. The model was simulated using the chemical engineering module and the dilute species

transportation module (version 4.3.0.151, COMSOL Inc.). The parameters used in the simulation are listed in Table I unless otherwise indicated.

*Water radiolysis.*— The interaction of α-radiation with water yields a series of decomposition products ($H_2$, $H_2O_2$, $H^\bullet$, $OH^\bullet$, $HO_2^\bullet$, $e_{aq}^-$, $H^+$ and $OH^-$), among which the molecular species are dominant. The radical species have concentrations orders of magnitude lower than those of the stable molecular products as a consequence of their high reactivity and consequently short lifetimes. Fig. 3 shows the concentration profiles for the radiolytic species $e_{aq}^-$, $H^\bullet$, $OH^\bullet$, $H_2O_2$, $H_2$, and $UO_2^{2+}$ and $Fe^{2+}$ inside a crack (width = 0.1 mm, depth = 1 mm) calculated using a full radiolytic reaction set. In this calculation the $H_2$ distribution includes a contribution from $H_2$ produced by steel corrosion ($[H_2]_{bulk} = 0.01$ µmol L$^{-1}$). Since the radical species ($H^\bullet$, $OH^\bullet$) and $e_{aq}^-$ are highly reactive with short ranges in water, they can only be found near the radiation zone on the fuel surface. By contrast, the molecular/ionic species ($H_2O_2$, $H_2$, $UO_2^{2+}$) have much higher concentrations than radical species. The radiolytic $H_2O_2$ and $H_2$ are accumulated within the fuel cracks, which accounts for the depletion of the radical species in these locations. At the concentration adopted ($[Fe^{2+}]_{bulk} = 0.01$ µmol L$^{-1}$), the $Fe^{2+}$ from the steel surface is almost completely consumed before entering the crack.

In the 1-D model,[34] a comparison between calculations conducted using a full α-radiolysis reaction set and those using a simplified approach in which only the radiolytic production of $H_2O_2/H_2$ are considered, showed the latter was acceptable with the advantage of a much shorter calculation time. This simplification is verified here for the 2-D case. The steady-state concentration profiles of $H_2O_2$, $H_2$ and $UO_2^{2+}$ calculated using both approaches are plotted in Fig. 4 as a function of distance along the center line of a crack; i.e., the vertical line down the middle of the crack from the base of the crack ($x = 0$ mm), through the crack mouth ($x = 1$ mm) to the diffusion boundary ($x = 2$ mm). Since the concentrations of the molecular/ionic species vary only marginally in the lateral direction (Fig. 3), Fig. 4 shows the concentration profiles calculated inside a crack. In general, both the radiolytic $H_2O_2$ and $H_2$ and the corrosion product, $UO_2^{2+}$, are at

**Table I. Default values of simulation parameters.**

| Parameter | Symbol | Value | Units |
|---|---|---|---|
| Diffusion layer thickness[49] | $L$ | 1 | mm |
| Radiation zone thickness[50] | $b$ | 13 | µm |
| Alpha radiation dose rate[a,50] | $D_R$ | $9.03 \times 10^5$ | Gy a$^{-1}$ |
| ε-particle coverage[28] | $s_\varepsilon$ | 0.01 | – |
| $H_2$ bulk concentration | $[H_2]_{bulk}$ | 0.01 | µmol L$^{-1}$ |
| $Fe^{2+}$ bulk concentration | $[Fe^{2+}]_{bulk}$ | 0.01 | µmol L$^{-1}$ |
| g-value of $H_2O_2$[b,34] | $g_{H2O2}$ | 0.1248 | µmol J$^{-1}$ |
| g-value of $H_2$[27] | $g_{H2}$ | 0.1248 | µmol J$^{-1}$ |
| $UO_2$ pellet oxidation rate constant in $H_2O_2$[32] | $k_{2a}$ | $1.0 \times 10^{-8}$ | m s$^{-1}$ |
| $H_2O_2/UO_2$ surface reaction rate constant on ε[14] | $k_{2b}$ | $6.92 \times 10^{-6}$ | m s$^{-1}$ |
| $H_2/U^{VI}$ surface reaction rate constant on ε[52] | $k_{3a}$ | $4 \times 10^{-7}$ | m s$^{-1}$ |
| $H_2/UO_2^{2+}$ bulk reaction rate constant[30] | $k_{3b}$ | $3.6 \times 10^{-9}$ | L mol$^{-1}$ s$^{-1}$ |
| $H_2/UO_2^{2+}$ surface reaction rate constant on ε[31] | $k_{3c}$ | $1.5 \times 10^{-5}$ | m s$^{-1}$ |
| $H_2/H_2O_2$ surface reaction rate constant on ε[29] | $k_4$ | $2.2 \times 10^{-5}$ | m s$^{-1}$ |
| $Fe^{2+}$ bulk reaction rate constant[53] | $k_5$ | $1 \times 10^6$ | L mol$^{-1}$ s$^{-1}$ |
| $H_2O_2$ homogeneous decomposition rate constant[54] | $k_{6a}$ | $8.29 \times 10^{-8}$ | s$^{-1}$ |
| $H_2O_2$ surface-catalyzed decomposition rate constant[c,32] | $k_{6b}$ | $6.14 \times 10^{-8}$ | m s$^{-1}$ |

[a]The unit Gy a$^{-1}$ is the absorbed dose per annum. One gray (Gy) is the absorption of one joule of energy, in the form of ionizing radiation, per kilogram of matter.
[b]According to Pastina et al.[27] the g-values are 0.104 µmol J$^{-1}$ for $H_2O_2$ and 0.1248 µmol J$^{-1}$ for $H_2$. The simplified calculation used in this model conservatively assumes all the other radiolytic radicals are recombined to produce $H_2O_2$ ($2OH^\bullet \rightarrow H_2O_2$, $H^\bullet + HO_2^\bullet \rightarrow H_2O_2$) and the overall g-value of $H_2O_2$ is assumed to be 0.1248 µmol J$^{-1}$ considering the mass balance during the radiolytic decomposition ($2H_2O \rightarrow H_2 + H_2O_2$). This simplification has been verified.[34]
[c]The rate constant for the surface catalyzed decomposition of $H_2O_2$ was calculated using the rate constant for $UO_2$ oxidation and the dissolution yield (14%) measured on a $UO_2$ pellet.[32] The dissolution yield was based on the ratio between the amount of dissolved $[U^{VI}]$ and the $H_2O_2$ consumed. The difference (86%) was attributed to catalytic decomposition of $H_2O_2$, from which the decomposition rate constant can be calculated.
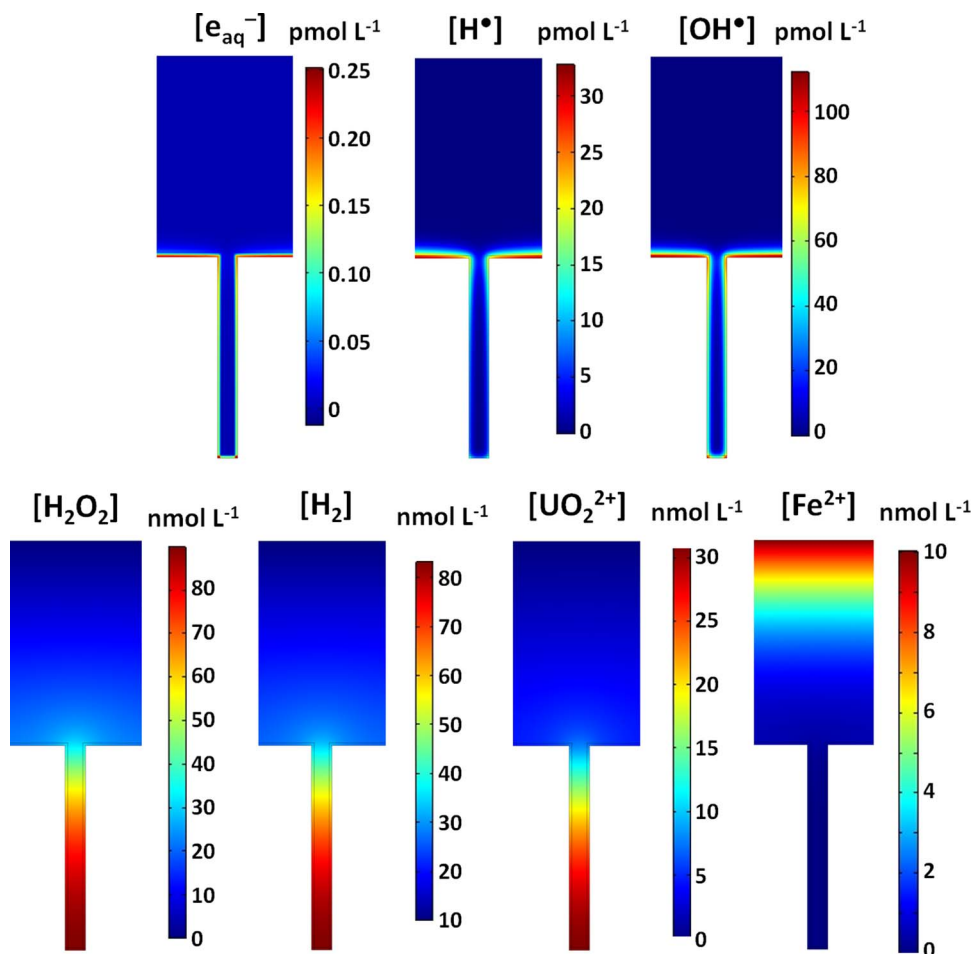
**Figure 3.** Concentration profiles for the radiolytic species, $e_{aq}^-$, $H^\bullet$, $OH^\bullet$, $H_2O_2$, $H_2$, and corrosion species, $UO_2^{2+}$ and $Fe^{2+}$, inside a crack (width = 0.1 mm, depth = 1 mm) calculated using a full radiolytic reaction set. $[H_2]_{bulk} = [Fe^{2+}]_{bulk} = 0.01$ µmol $L^{-1}$.

their maximum concentrations at the base of the crack and rapidly decrease as the crack mouth is approached. Beyond the crack mouth the concentrations slowly decrease to the bulk solution values at the diffusion boundary. The estimated $[H_2O_2]$ and $[UO_2^{2+}]$ calculated
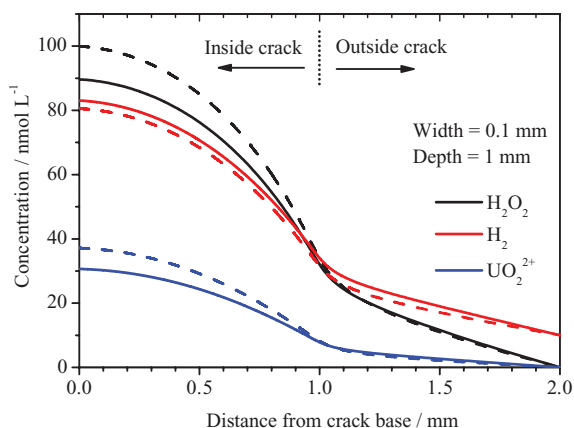


**Figure 4.** The calculated steady-state $[H_2]$, $[H_2O_2]$ and $[UO_2^{2+}]$ as a function of the distance from the base of a crack, along the center line of the crack, to the diffusion boundary located 1 mm from the crack mouth. The solid lines are the values calculated using a full radiolysis reaction set, and the dashed lines are the estimated concentrations based on the radiolytic production of only $H_2O_2$ and $H_2$. Crack width = 0.1 mm; crack depth = 1 mm; $[H_2]_{bulk}$ = $[Fe^{2+}]_{bulk} = 0.01$ µmol $L^{-1}$.

from the radiolytic production of only $H_2O_2/H_2$ (dashed lines) are 10 to 20% higher than the values calculated using a full radiolysis reaction set (solid lines). For the $[H_2]$ the difference between the two calculations is marginal (<3%). These differences are consistent with those obtained in the 1-D model[34] and the estimated corrosion rates can be considered slightly conservative.

The crack geometry used in this example is relatively compact (width = 0.1 mm, depth = 1 mm) which allows the effect of the radicals to be visible. However, for wider/deeper cracks the impact of radical species will be even smaller, and it can be concluded that using only the radiolytic production of $H_2O_2$ and $H_2$ to simulate α-radiolysis is an acceptable estimation for the 2-D model. All the data in the following sections are calculated using this simplified radiolysis approach.

*Effect of $H_2$.*— The previous 1D model[34,49] showed that $H_2$ can completely suppress $UO_2$ corrosion on a planar fuel surface. The critical $[H_2]$ required for the complete inhibition of corrosion, $[H_2]_{crit}$, was calculated to be ~0.19 µmol $L^{-1}$ for CANDU fuel with an age of 1000 years. Since the crack geometry can lead to the local accumulation of radiolysis species, Fig. 3, the $[H_2]_{crit}$ for a 2-D crack is expected to be different from that calculated for a planar surface. Fig. 5 shows the $[H_2]$ and $[H_2O_2]$ profiles along the center line of a crack as a function of increasing $[H_2]_{bulk}$. The $[H_2]$ is a maximum at the base of the crack and decreases along the diffusion pathway. As the $[H_2]_{bulk}$ increases, the total $[H_2]$ rises at all locations along the diffusion pathway, the increase being proportional to the increase in $[H_2]_{bulk}$, suggesting the concentrations of the external and radiolytically-
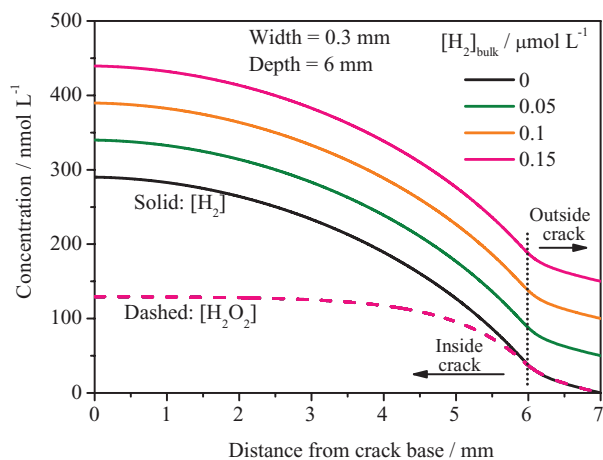
**Figure 5.** The [$H_2$] and [$H_2O_2$] as a function of the distance from the base of a crack calculated along the center line of the crack, to the diffusion boundary located 1 mm from the mouth of the crack, at various [$H_2$]$_{bulk}$. Crack width = 0.3 mm; crack depth = 6 mm; [$Fe^{2+}$]$_{bulk}$ = 0.01 $\mu$mol L$^{-1}$.



**Figure 6.** The calculated diffusive flux of $UO_2^{2+}$ (corrosion rate) in the direction normal to the wall of the crack as a function of the distance from the base of the crack at various [$H_2$]$_{bulk}$. Crack width = 0.3 mm; crack depth = 6 mm; [$Fe^{2+}$]$_{bulk}$ = 0.01 $\mu$mol L$^{-1}$.

produced $H_2$ are additive. On the other hand, the [$H_2O_2$] is almost constant within the crack and decreases rapidly around and beyond the mouth of the crack due to its diffusion out of the crack and consumption by reaction with $Fe^{2+}$. The [$H_2O_2$] profile is independent of [$H_2$]$_{bulk}$, for a number of reasons. Firstly, by adopting the simplified radiolysis approach, the reactions between radiolytic $H_2O_2$ and $H_2$ and other species involved in the full radiolysis reaction set are not included, for example,

$$OH^\bullet + H_2 \longrightarrow H_2O + H^\bullet \qquad [2]$$

$$H^\bullet + H_2O_2 \longrightarrow H_2O + OH^\bullet \qquad [3]$$
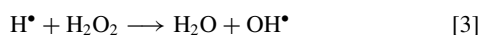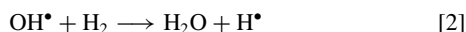
However, our previous calculations[34] show that neglecting these reactions makes only a marginal difference in [$H_2O_2$] for the low [$H_2$]$_{bulk}$ used here. This approximation is justified since experimental/modeling studies have shown that the presence of small concentrations ($\sim\mu$mol L$^{-1}$) of $H_2$ have only a minor effect on $H_2O_2$ production by $\alpha$-radiolysis.[27,28] Secondly, although the present model includes the surface-catalyzed reaction between $H_2O_2$ and $H_2$, reaction 4 in Fig. 1,

$$H_2O_2 + H_2 \xrightarrow{\varepsilon} 2H_2O \qquad [4]$$

the rate of this reaction has been shown to be independent of [$H_2$].[29]

The highest value of [$H_2$] shown in Fig. 5 is 440 nmol L$^{-1}$ at the base of the crack, which is $\sim$3 times that of [$H_2O_2$] at this location. Considering that the primary yields (g-values, Table I) of $H_2O_2$ and $H_2$ are the same, this difference can be attributed to a number of features; (i) the externally supplied $H_2$; (ii) $H_2$ is stable whereas a major pathway for $H_2O_2$ consumption is its decomposition;[6,32] and (iii) $H_2O_2$ and $H_2$ react at different rates with the fuel surface.[34] The balance between [$H_2O_2$] and [$H_2$] will influence the competition between the $UO_2$ oxidation by $H_2O_2$ and its reduction by $H_2$.

In the 2-D simulation, the diffusive flux of $UO_2^{2+}$ in the direction normal to the fuel surface is equivalent to the $UO_2$ corrosion rate. Fig. 6 plots the flux on the inside walls of the crack for the same conditions as those used in Fig. 5. The corrosion rate exhibits a maximum value near the mouth of the crack, and approaches zero at the base of the crack, indicating a very significant suppression of corrosion within the crack. Since the access of the external reductants ($Fe^{2+}$ and $H_2$) to deep locations within the crack is limited, this suppression can be attributed to the local accumulation of radiolytic $H_2$, which is highest at the base of the crack resulting in a negligible corrosion rate. As the [$H_2$] decreases along the crack while the [$H_2O_2$] remains close to constant for $x < 4$ mm (Fig. 5), the corrosion rate increases. The rapid decrease in rate as the crack mouth is approached is due to the rapid
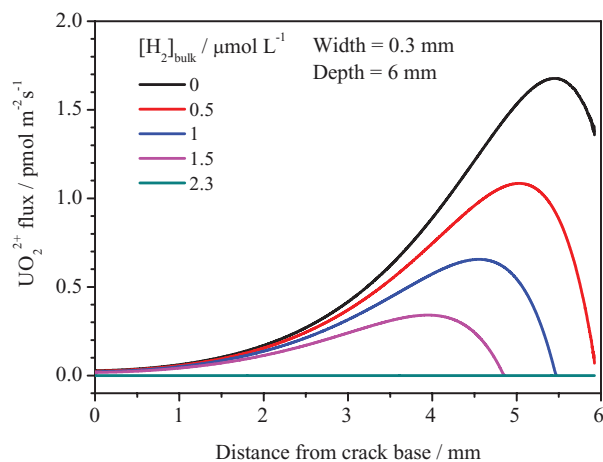
decrease in [$H_2O_2$] as it diffuses out of the crack and is consumed by the Fenton reaction as external $Fe^{2+}$ diffuses in.

To obtain the [$H_2$]$_{crit}$, the $UO_2^{2+}$ flux in the direction normal to the fuel surface was calculated as a function of increasing [$H_2$]$_{bulk}$. The [$H_2$]$_{crit}$ is taken to be achieved when corrosion is completely suppressed at all surface locations. For the crack dimensions assumed in Fig. 6 (width = 0.3 mm, depth = 6 mm), the $UO_2^{2+}$ flux decreases with increasing [$H_2$]$_{bulk}$ and drops to zero at all locations for [$H_2$]$_{crit}$ = 2.3 $\mu$mol L$^{-1}$.

To simulate a range of crack geometries, different combinations of widths (0.1–3 mm) and depths (0.5–9 mm) were chosen based on the dimensions of cracks shown to occur in used fuel pellets.[39] The calculated [$H_2$]$_{crit}$ values for different geometries are plotted in Fig. 7. As Fig. 7 shows the [$H_2$]$_{crit}$ increases to a peak value and then decreases as the crack deepens. This is obvious in Fig. 7 for crack widths <1 mm, while for a crack width >1 mm the peak appears at deeper locations (>10 mm). It is generally expected that the required [$H_2$]$_{crit}$ would be larger for deeper cracks. However, as Fig. 7 demonstrates, when the crack is sufficiently deep, the [$H_2$]$_{crit}$ increases only marginally and even decreases slightly, suggesting a significant suppression of radiolytic corrosion. This can be partially attributed to the local accumulation of radiolytic $H_2$, as indicated by Fig. 5. This is important as
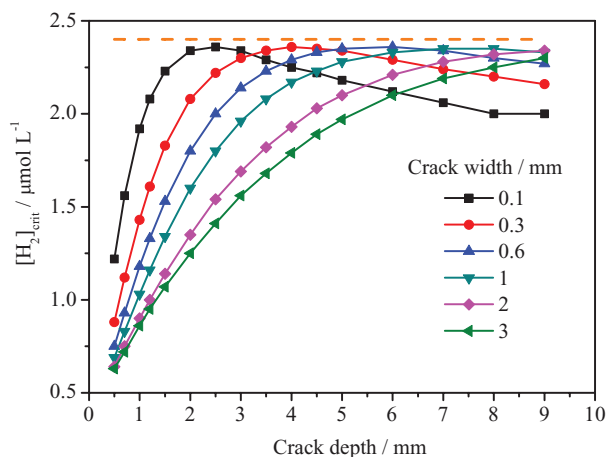


**Figure 7.** The calculated [$H_2$]$_{crit}$ required to completely suppress fuel corrosion in cracks with different widths and depths. [$Fe^{2+}$]$_{bulk}$ = 0.01 $\mu$mol L$^{-1}$. The dashed line indicates an upper limit, 2.4 $\mu$mol L$^{-1}$, for [$H_2$]$_{crit}$.
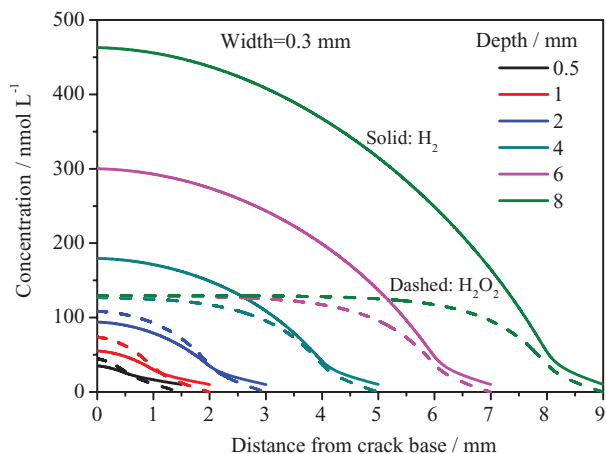
**Figure 8.** The calculated [$H_2$] and [$H_2O_2$] as a function of the distance from the base of a crack along the center line of the crack, and beyond the crack mouth to the diffusion boundary (1 mm from the mouth), for different crack depths and a constant width (0.3 mm); [$H_2$]$_{bulk}$ = [$Fe^{2+}$]$_{bulk}$ = 0.01 $\mu$mol L$^{-1}$.



**Figure 9.** The calculated diffusive flux of $UO_2^{2+}$ (the corrosion rate) in the direction normal to the walls of the crack as a function of the distance from the base of the crack, for different crack depths and a constant width (0.3 mm); [$H_2$]$_{bulk}$ = [$Fe^{2+}$]$_{bulk}$ = 0.01 $\mu$mol L$^{-1}$.

it suggests there exists an upper limit (2.4 $\mu$mol L$^{-1}$ indicated by the dashed line in Fig. 7) for [$H_2$]$_{crit}$ for the anticipated range of possible crack geometries. This value is ~12 times the [$H_2$]$_{crit}$ required on the planar uncracked surface.[34] On the other hand, in the extreme case when the crack depth approaches zero, i.e., the crack is essentially eliminated, the [$H_2$]$_{crit}$ should approach the value calculated for the planar fuel (~0.19 $\mu$mol L$^{-1}$).[34]

*Effect of crack depth.*— Fig. 8 shows the [$H_2$] and [$H_2O_2$] profiles along the center line of the crack for a constant width (0.3 mm) as a function of depth. The accumulation of radiolytic $H_2$ results in a significant build up in [$H_2$] as the crack becomes deeper. For a crack depth = 8 mm, the highest [$H_2$] is 460 nmol L$^{-1}$ at the base which is 10 times that for a crack only 0.5 mm deep. The other radiolytic product, $H_2O_2$, also exhibits a maximum concentration at the base of the crack which rises as the depth increases from 0.5 to ~3 mm. For depths >3 mm, the [$H_2O_2$] achieves a plateau value at the base and the increase of [$H_2O_2$]$_{max}$ becomes marginal to insignificant. Since the rates of radiolytic production (g-values) are the same for $H_2O_2$ and $H_2$, this difference reflects the more rapid consumption of $H_2O_2$ compared to $H_2$ as noted above. Since the $Fe^{2+}$ from the bulk solution is rapidly eliminated along the diffusion pathway (Fig. 3), the Fenton reaction (reaction 5 in Fig. 1) has only a minor influence on [$H_2O_2$] inside a deep crack, at least for the [$Fe^{2+}$]$_{bulk}$ adopted in this model. The catalytic reaction between $H_2O_2$ and $H_2$ (reaction 4 in Fig. 1) will result in equal consumption rates for both reactants, and cannot contribute to the difference between [$H_2O_2$] and [$H_2$]. Consequently, the main reasons for this difference are, (i) the high consumption rate of $H_2O_2$ in the corrosion reaction (reaction 2 in Fig. 1) which proceeds by both direct reaction of $UO_2$ with $H_2O_2$ and the galvanically-coupled $UO_2$ oxidation by $H_2O_2$ reduction on noble metal ($\varepsilon$) particles;[52] and (ii) the extensive surface decomposition of $H_2O_2$, which accounts for 86% of total $H_2O_2$ consumption on the $UO_2$ surface.[32] The influence of the decomposition product, $O_2$, is also included in the model. However, sensitivity calculations show its inclusion has no significant effect on the fuel corrosion rate. This is not unexpected since the rate constant for the reaction between $O_2$ and $UO_2$ is 1/200$^{th}$ that of the reaction between $H_2O_2$ and $UO_2$.[4]

The $UO_2^{2+}$ flux (corrosion rate) on the wall of a crack is plotted as a function of crack depth in Fig. 9. For a crack depth ≤1 mm, the maximum corrosion rate occurs at the base of the crack, since the [$H_2$] is low compared to [$H_2O_2$], as shown in Fig. 8. For crack depths >2 mm, the [$H_2O_2$] is decreased and the difference between [$H_2$]

especially near the base of the crack where [$H_2$] is high. For a crack depth = 8 mm, the corrosion rate becomes zero within 2.5 mm of the crack base; i.e., the $UO_2$ surface does not corrode. Interestingly, the maximum $UO_2^{2+}$ flux (corrosion rate) near the crack mouth becomes constant for crack depths ≥ 4 mm. This could account for the marginal increase (or slight decrease) in [$H_2$]$_{crit}$ for deep cracks observed in Fig. 7, since the maximum corrosion rate will be the dominant influence determining the [$H_2$]$_{crit}$ required to completely suppress the corrosion process.

*Effect of crack width.*— Fig. 10 shows the calculated [$H_2$] and [$H_2O_2$] profiles along the center line of cracks with different widths and a constant depth (6 mm). For the widest crack (width = 3 mm), the [$H_2O_2$] is slightly higher than [$H_2$], which is consistent with the trend obtained on a planar surface; i.e., if its width is sufficiently large, the crack becomes unnoticeable and the concentration profiles approach those of a planar surface. As the crack becomes narrower, the [$H_2$] significantly increases, whereas the [$H_2O_2$] only increases slightly and reaches a plateau (~130 nmol L$^{-1}$) near the base of the crack.

The rapid increase in [$H_2$] as the crack width decreases reflects the approach of the total crack volume to that of the irradiated zone, and the decrease in diffusive loss of $H_2$ from the crack. By contrast



**Figure 10.** The calculated [$H_2$] and [$H_2O_2$] as a function of the distance from the base of a crack, along the center line of the crack, to the diffusion boundary located 1 mm from the crack mouth, for different crack widths and a constant depth (6 mm); [$H_2$]$_{bulk}$ = [$Fe^{2+}$]$_{bulk}$ = 0.01 $\mu$mol L$^{-1}$.
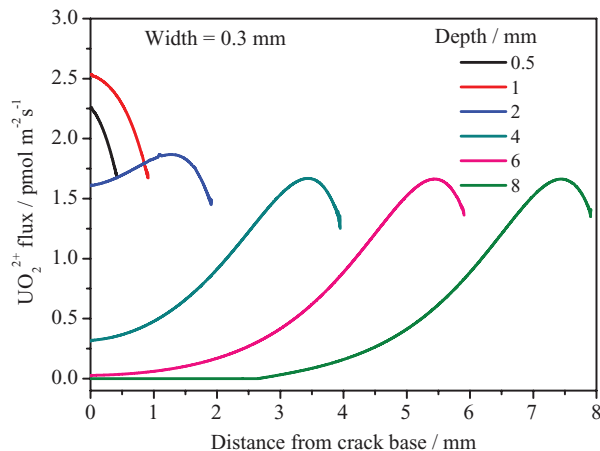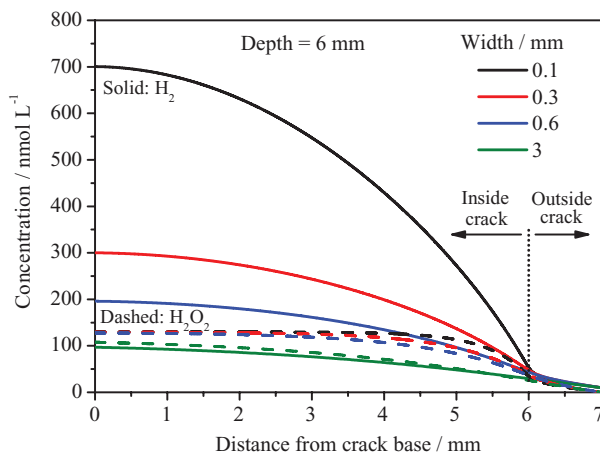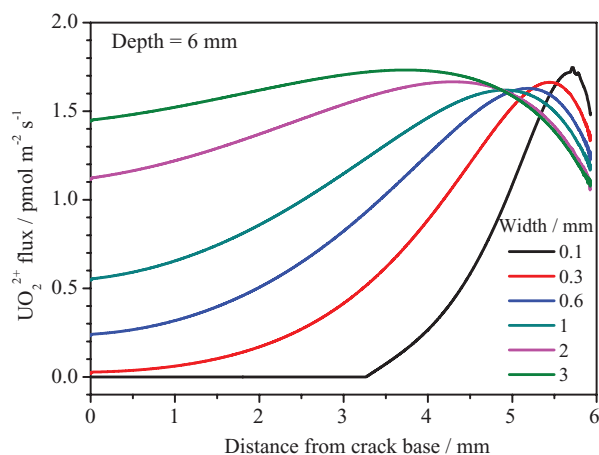
**Figure 11.** The calculated diffusive flux of $UO_2^{2+}$ (corrosion rate) in the direction normal to the walls of the crack as a function of the distance from the base of the crack, for different crack widths and a constant depth (6 mm); $[H_2]_{bulk} = [Fe^{2+}]_{bulk} = 0.01 \, \mu mol \, L^{-1}$.

the $[H_2O_2]$ remains low for the reasons discussed above (Section 3.3). The pronounced difference between $[H_2]$ and $[H_2O_2]$ inside the crack will subsequently suppress the $UO_2$ corrosion.

The $UO_2^{2+}$ flux (corrosion rate) at the walls of a crack are plotted for different widths in Fig. 11. Over the majority of the wall, the corrosion rate decreases as the crack width decreases from 3 mm to 0.1 mm. For a narrow crack (0.1 mm), the corrosion rate within 3.3 mm from the base is virtually zero, as a consequence of the high $[H_2]$ (∼6 times the $[H_2O_2]$, Fig. 10). As the crack width increases, the maximum corrosion rate varies very little, but its location within the crack shifts slightly to deeper locations. This minor change in maximum corrosion rate with crack width is reflected in the small change in $[H_2]_{crit}$ required to suppress corrosion, Fig. 7.

## Conclusions

A 2-D model has been developed to predict the corrosion rate of spent fuel within cracks in a nuclear fuel pellet. The influence of α-radiolysis can be accounted for using a simplified calculation which only accounts for the radiolytic production of $H_2O_2$ and $H_2$. This produces slightly conservative values for the $UO_2$ corrosion rate, only overestimating $H_2O_2$ production and $UO_2$ corrosion rates by ∼10–20%. This simplification shortens calculation times considerably.

The $Fe^{2+}$ produced by corrosion of the steel vessel was found to exert a minor influence at the assumed concentration (0.01 $\mu mol \, L^{-1}$), via the Fenton reaction, on the $[H_2O_2]$ within a crack and hence on the corrosion rate.

Both $H_2O_2$ and $H_2$ were found to accumulate inside cracks. The $[H_2O_2]$ was suppressed in deep cracks due to its rapid consumption by the corrosion reaction and, especially, its decomposition to $O_2$ and $H_2O$. By contrast, the radiolytic $[H_2]$ increased significantly as the crack became deeper and/or narrower.

This accumulation of radiolytic $H_2$ leads to the suppression of corrosion especially within deep cracks. The influence of external $H_2$ on the corrosion rate was confined to regions close to the mouth of the crack.

The critical $[H_2]$, $[H_2]_{crit}$, required to completely suppress corrosion was calculated for various crack widths and depths. As the crack becomes deeper $[H_2]_{crit}$ increases and then decreases. This indicates there is an upper limiting value for $[H_2]_{crit}$ for cracks of the observed dimensions in spent fuels. The maximum value for CANDU fuel with a burnup of 220 MWh kgU$^{-1}$ and an age of 1000 years (after discharge from reactor) is 2.4 $\mu mol \, L^{-1}$, which is ∼12 times higher than the $[H_2]_{crit}$ required on a planar uncracked fuel surface.

These calculations indicate that the conditions within cracks begin to decouple from those existing outside the crack as the crack deepens. Since $H_2O_2$ is consumed within the crack, primarily by its decomposition, while $H_2$ is not, redox conditions become progressively more reducing and fuel corrosion is significantly suppressed and even eliminated.

While these calculations do not fully capture the chemistry within a corroding crack they suggest that radiolytic corrosion in deep cracks in the fuel may not be as aggressive as originally feared and that a connection to the external reducing conditions established by the corroding steel vessel may be less important than originally envisaged.

## References

1. J. McMurry, D. A. Dixon, J. D. Garroni, B. M. Ikeda, S. Stroes-Gascoyne, P. Baumgartner, and T. W. Melnyk, *Ontario Power Generation*, Report 06819-REP-01200-10092-R00, Toronto, ON (2003).
2. F. King and M. Kolar, *Ontario Power Generation*, Report 06819-REP-01200-10041-R00, Toronto, ON (2000).
3. F. King, C. Lilja, K. Pedersen, P. Pitkänen, and M. Vähänen, *Swedish Nuclear Fuel and Waste Management Co. (SKB)*, Report TR-10-67, Stockholm, Sweden (2010).
4. D. W. Shoesmith, *J. Nucl. Mater.*, **282**, 1 (2000).
5. E. Ekeroth, O. Roth, and M. Jonsson, *J. Nucl. Mater.*, **355**(1-3), 38 (2006).
6. C. M. Lousada, M. Trummer, and M. Jonsson, *J. Nucl. Mater.*, **434**, 434 (2013).
7. D. W. Shoesmith, *Nuclear Waste Management Organization*, Report NWMO TR-2007-03, Toronto, ON (2007).
8. D. W. Shoesmith, *Nuclear Waste Management Organization*, Report NWMO TR-2008-19, Toronto, ON (2008).
9. G. M. Kwong, *Nuclear Waste Management Organization*, Report NWMO TR-2011-14, Toronto, ON (2011).
10. T. E. Eriksen, D. W. Shoesmith, and M. Jonsson, *J. Nucl. Mater.*, **420**, 409 (2012).
11. J. W. T. Spinks and R. J. Woods, *An Introduction to Radiation Chemistry*, The Third Edition, John Wiley & Sons Inc., New York (1990).
12. M. E. Broczkowski, D. Zagidulin, and D. W. Shoesmith, in "Nuclear Energy and the Environment, American Chemical Society Symposium," Vol. 1046, Chapter 26, p. 349–380, 2010.
13. P. Carbol, J. Cobos-Sabate, J.-P. Glatz, C. Ronchi, V. Rondinella, D. H. Wegen, T. Wiss, A. Loida, V. Metz, B. Kienzler, K. Spahiu, B. Grambow, J. Quinones, and A. Martinez Esparza Valiente, *Swedish Nuclear Fuel and Waste Management Co. (SKB)*, Report TR-05-09, Stockholm, Sweden (2005).
14. M. Trummer, O. Roth, and M. Jonsson, *J. Nucl. Mater.*, **383**, 226 (2009).
15. P. G. Lucuta, R. A. Verrall, H.-J. Matzke, and B. J. F. Palmer, *J. Nucl. Mater.*, **178**, 48 (1991).
16. H. Kleykamp, *J. Nucl. Mater.*, **131**, 221 (1985).
17. H. Kleykamp, *J. Nucl. Mater.*, **206**, 82 (1993).
18. P. Carbol, P. Fors, S. Van Winckel, and K. Spahiu, *J. Nucl. Mater.*, **392**, 45 (2009).
19. K. Spahiu, L. O. Werme, and U. B. Eklund, *Radiochim. Acta*, **88**, 507 (2000).
20. K. Spahiu, D. Cui, and M. Lundström, *Radiochim. Acta*, **92**, 625 (2004).
21. S. Röllin, K. Spahiu, and U. B. Eklund, *J. Nucl. Mater.*, **297**(3), 231 (2001).
22. E. Cera, J. Bruno, L. Duro, and T. E. Eriksen, *Swedish Nuclear Fuel and Waste Management Co (SKB)*, Report TR-06-07, Stockholm, Sweden (2006).
23. A. Traboulsi, J. Vandenborre, G. Blain, B. Humbert, J. Barbet, and M. Fattahi, *J. Phys. Chem. C*, **118**, 1071 (2013).
24. M. E. Broczkowski, J. J. Noël, and D. W. Shoesmith, *J. Nucl. Mater.*, **346**, 16 (2005).
25. M. E. Broczkowski, J. J. Noël, and D. W. Shoesmith, *J. of Electroanal. Chem.*, **602**, 8 (2007).
26. M. E. Broczkowski, P. G. Keech, J. J. Noël, and D. W. Shoesmith, *J. Electrochem. Soc.*, **157**(8), C275 (2010).
27. B. Pastina and J. A. LaVerne, *J. Phys. Chem. A*, **105**, 9316 (2001).
28. M. Trummer and M. Jonsson, *J. Nucl. Mater.*, **396**(2–3), 163 (2010).
29. S. Nilsson and M. Jonsson, *J. Nucl. Mater.*, **372**, 160 (2008).
30. E. Ekeroth, M. Jonsson, T. E. Eriksen, K. Ljungqvist, S. Kovacs, and I. Puigdomenech, *J. Nucl. Mater.*, **334**(1), 35 (2004).
31. S. Nilsson and M. Jonsson, *J. Nucl. Mater.*, **374**, 290 (2008).
32. R. Pehrman, M. Trummer, C. M. Lousada, and M. Jonsson, *J. Nucl. Mater.*, **430**, 6 (2012).
33. M. Jonsson, F. Nielsen, O. Roth, E. Ekeroth, S. Nilsson, and M. M. Hossain, *Environmental Science & Technology*, **41**(20), 7087 (2007).
34. L. Wu, Z. Qin, and D. W. Shoesmith, *Corros. Sci.*, **84**, 85 (2014).
35. C. Poinssot, C. Ferry, M. Kelm, B. Grambow, A. Martinez Esparza Valiente, L. H. Johnson, Z. Andriambololona, J. Bruno, C. Cachoir, J.-M. Cavedon, H. Christensen, C. Corbel, C. Jegou, K. Lemmens, A. Loida, P. Lovera, F. Miserque,

J. de Pablo, A. Poulesquen, J. Quinones, V. Rondinella, K. Spahiu, and D. H. Wegen, *CEA*, Report CEA-R-6093, collective work (2005).

36. H. Christensen, S. Sunder, and D. W. Shoesmith, *J. Alloys Compd.*, **213/214**, 93 (1994).
37. A. Poulesquen and C. Jegou, *Nucl. Tech.*, **160**, 337 (2007).
38. D. W. Shoesmith, M. Kolar, and F. King, *Corrosion*, **59**(9), 802 (2003).
39. K. M. Wasywich, W. H. Hocking, D. W. Shoesmith, and P. Taylor, *Nucl. Tech.*, **104**, 309 (1993).
40. E. Kohn, G. I. Hadaller, R. M. Sawala, G. H. Archinoff, and S. L. Wadsworth, in: *the Sixth Canadian Nuclear Society Conference Proceedings*, Ottawa, ON (1985).
41. M. Oguma, *Nuclear Engineering and Design*, **76**, 35 (1983).
42. J. D. Higgs, B. J. Lewis, W. T. Thompson, and Z. He, *J. Nucl. Mater.*, **366**, 99 (2007).
43. D. E. Olander, *Fundamental Aspects of Nuclear Reactor Fuel Elements*, ERDA, U.S. (1976).
44. C. Bernaudat, *Nuclear Engineering and Design*, **156**, 373 (1995).
45. I. J. Hastings, *Atomic Energy of Canada Limited*, Report AECL-MISC-249, Chalk River, ON (1982).
46. J. Novak and I. J. Hastings, *Atomic Energy of Canada Limited*, Report AECL-10388, Chalk River, ON (1991).
47. J. Bruno and R. C. Ewing, *Elements*, **2**, 343 (2006).
48. G. Khvostov, K. Mikityuk, and M. A. Zimmermann, *Nuclear Engineering and Design*, **241**(8), 2983 (2011).
49. L. Wu, Y. Beauregard, Z. Qin, S. Rohani, and D. W. Shoesmith, *Corros. Sci.*, **61**, 83 (2012).
50. F. Garisto, D. H. Barber, E. Chen, A. Inglot, and C. A. Morrison, *Nuclear Waste Management Organization*, Report NWMO TR-2009-27, Toronto, ON (2009).
51. A. Poulesquen, C. Jégou, and S. Peuget, in *Scientific Basis for Nuclear Waste Management XXIX.*, P. Van Iseghem, ed., p. 505-512, Material Research Society (Mater. Res. Soc. Symp. Proc. 932), Warrendale, PA (2006).
52. M. Trummer, S. Nilsson, and M. Jonsson, *J. Nucl. Mater.*, **378**(1), 55 (2008).
53. F. J. Millero and S. Sotolongo, *Geochim. Cosmochim. Acta*, **53**, 1867 (1989).
54. A. J. Elliot and D. M. Bartels, *Atomic Energy of Canada Limited*, Report 153-127160-450-001, Mississauga, ON (2009).